The 2016 Kaikōura, New Zealand, Earthquake: Preliminary Seismological Report

by A. Kaiser, N. Balfour, B. Fry, C. Holden, N. Litchfield, M. Gerstenberger, E. D'Anastasio, N. Horspool, G. McVerry, J. Ristau, S. Bannister, A. Christophersen, K. Clark, W. Power, D. Rhoades, C. Massey, I. Hamling, L. Wallace, J. Mountjoy, Y. Kaneko, R. Benites, C. Van Houtte, S. Dellow, L. Wotherspoon, K. Elwood, and K. Gledhill

ABSTRACT

The 2016 M_w 7.8 Kaikōura earthquake continued a notable decade of damaging earthquake impacts in New Zealand. The effects were wide ranging across the upper South Island, and included two fatalities, tsunami, tens of thousands of landslides, the collapse of one residential building, and damage to numerous structures and infrastructure. We present a preliminary overview focused on the seismological aspects of this earthquake and the corresponding seismological response effort. The earthquake rupture was extremely complex, involving at least 13 separate faults extending over ~150 km, from the epicenter in north Canterbury to near the Cook Strait. We use backprojection and slip inversion methods to derive preliminary insights into the rupture evolution, identifying south-to-north rupture, including at least three distinct southwest-to-northeast propagating phases. The last phase is associated with a strong second pulse of energy release in the northern half of the rupture zone ~70 s after rupture initiation, which we associate with the Kekerengu–Needles faults where some of the largest surface displacements (dextral) were observed. The mechanism of the mainshock was oblique thrust and relocated aftershocks show a range of thrust and strike-slip mechanisms across three dominant spatial clusters. GeoNet datasets collected during the Kaikōura earthquake will be crucial in further unraveling details of the complex earthquake rupture and its implications for seismic hazard. Ground motions during the earthquake exceeded 1*g* at both ends of the rupture. Spectral accelerations exceeded 500-year return period design level spectra in numerous towns in the upper South Island, as well as in parts of the capital city of Wellington at critical periods of 1–2 s, influenced by site/basin and directivity effects. Another important part of the response effort has been the provision of earthquake forecasts, as well as consideration of the implications of slow slip on the Hikurangi subduction interface triggered as a result of the Kaikōura earthquake.

INTRODUCTION

A moment magnitude (M_w) 7.8 earthquake struck the South Island of New Zealand at 12:03 a.m. local time on 14 November 2016 (Table 1). The epicenter was located ~4 km from the rural town of Waiau (population ~250) in north Canterbury (Fig. 1), and the rupture initiated at a shallow depth of 15 km. The earthquake ruptured a series of active faults, terminating offshore and severely impacting coastal and inland settlements across the northeast (NE) of the South Island.

The Kaikōura earthquake continues a decade in New Zealand's history of significant earthquake impacts. This follows a period since ~1950, suggestive of relative quiescence in the short ~150-year New Zealand historical record (e.g., Smith, 1981). The earthquake was the largest to strike New Zealand since the 2009 M_w 7.8 Dusky Sound earthquake on the Puysegur subduction interface at the southernmost extent of the country (Fry *et al.*, 2010; updated M_w is adopted from the USGS website, see Data and Resources). It also follows recent large earthquakes of M_w 6.6 to the north (2013 Cook Strait sequence, Holden *et al.*, 2013), as well as the 2010 M_w 7.1 Darfield earthquake and devastating Canterbury earthquake sequence to the south (Gledhill *et al.*, 2011; Kaiser *et al.*, 2012).

The effects of the Kaikōura earthquake on the population, infrastructure, and the environment were severe and wide ranging, with an estimated cost of NZ$3–8 billion for rebuild efforts. There were two fatalities in the worst-affected Hurunui and Kaikōura districts, in which damage was concentrated and a local state of emergency was declared. One of the fatalities resulted from the sole confirmed building collapse, the other reportedly resulted from a heart attack. Building damage due to shaking was also observed in larger towns further from the rupture, including Blenheim, and the central business district of the capital city of Wellington.

The coastal town of Kaikōura (population ~3500) was particularly badly affected, with all road and rail access routes initially closed due to landslides. The earthquake occurred in a region dominated by rugged mountainous terrain, which experienced an estimated tens of thousands of landslides of size ranging from a few cubic meters to millions of cubic meters of material. At least 190 landslide dams of significance have been

doi: 10.1785/0220170018

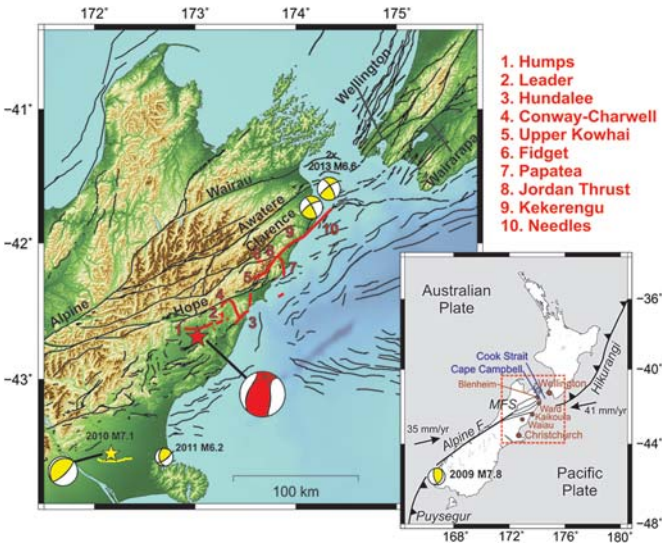

▲ **Figure 1.** Location of the Kaikōura earthquake epicenter (red star) and faults where surface rupture was observed (Hamling *et al.*, 2017; key faults numbered in red). Note that the Hope fault rupture was of small magnitude and only observed near the coast. New Zealand's active faults are plotted as black lines based on the onshore database of Langridge *et al.* (2016) and the offshore database of the National Institute of Water and Atmospheric Research Ltd. Major faults that did not rupture during the Kaikōura earthquake are labeled in black. Regional moment tensor solutions (GeoNet catalog) are plotted at the epicentral location of significant recent earthquakes: M_w 7.1 Darfield earthquake (epicenter shown by yellow star, surface rupture shown in yellow), M_w 6.2 Christchurch earthquake, M_w 6.6 Cook Strait and Lake Grassmere earthquakes, and M_w 7.8 Dusky Sound earthquake (inset). The inset shows a sketch of New Zealand's tectonic setting with the location of key settlements surrounding the Kaikōura rupture.

identified, of which 11 pose an ongoing risk to local communities and are being closely monitored.

One remarkable feature of the Kaikōura earthquake was the large number of faults that ruptured in a single earthquake. Surface rupture was observed on at least 13 different faults, with mapping efforts still underway (Hamling *et al.*, 2017, locations shown in Fig. 1). Surface rupture on submarine faults also generated a tsunami with local runup heights ranging up to at least 5 m and some localized damage. Understanding the complex fault interactions and kinematics will be an important topic of future research and has implications for our understanding of seismic hazard globally, in particular when accounting for multisegment and multifault ruptures in seismic-hazard models.

New Zealand's geological hazard monitoring centre (GeoNet, run by GNS Science) has captured valuable datasets from this earthquake that will enable better understanding of the event and its impacts. GeoNet earthquake parameters are summarized in Table 1. We present a preliminary report focusing on seismological aspects of the earthquake, including the source characteristics, kinematics of earthquake rupture, ground motions, and the implications for future hazard in the region.

TECTONIC SETTING AND PAST SEISMICITY

New Zealand's tectonic setting is characterized by two subduction systems of opposite polarity linked by an area of oblique continental convergence (Fig. 1). In the North Island, the Pacific plate subducts obliquely westward beneath the Australian plate at the Hikurangi subduction margin with relative plate motion of ~39–48 mm/yr increasing northward (Beavan *et al.*, 2016; Fig. 1). In contrast, central South Island tectonics are dominated by oblique continental convergence, with the majority of relative plate motion taken up along the transpressional plate-boundary Alpine fault, with dextral slip rates averaging up to ~25 mm/yr (Sutherland *et al.*, 2006; Norris and Cooper, 2007; Litchfield *et al.*, 2014). In the south of the country, eastward subduction dominates at the Puysegur margin.

The Kaikōura earthquake occurred in a tectonically complex area marking a transition from the southern Hikurangi subduction zone to continental convergence. The region is dominated by the Marlborough fault system (MFS), which includes four major southwest–northeast (SW–NE)-trending strike-slip faults that take up the majority of relative plate motion (Van Dissen *et al.*, 1991; Wallace *et al.*, 2012). These faults become progressively younger toward the south, with the highest slip rate (25 mm/yr; Langridge *et al.*, 2003) occurring on the southernmost Hope fault. A larger thrust component is evident on faults within the MFS striking in a more north–south direction.

Table 1
Kaikōura Earthquake Key Parameters

Epicenter	42.69° S, 173.02° E	GeoNet location calculated using broadband and selected strong-motion stations within 1.2° of the epicenter. GeoNet magnitude calculated using selected broadband stations up to 8° from the epicenter.
Depth	15 km	
Origin time (yyyy/mm/dd hh:mm:ss.ss)	2016/11/13 11:02:56.35 (UTC) 2016/11/14 12:02:56.35 (NZST)	
Moment magnitude	M_w 7.8	
Dominant mechanism	Oblique thrust	Adopted from Global Centroid Moment tensor (see Data and Resources)
Maximum modified Mercalli intensity	MMI IX	GeoNet ShakeMap

The subducted Pacific plate to the north also extends beneath the northern South Island, and has been imaged as far south as −42.5° (Eberhart-Phillips and Bannister, 2010). However, the southern extent of possible rupture on the subduction interface still remains unclear. The convergence rate at the trench decreases significantly southward along the Hikurangi margin (Wallace *et al.*, 2009, 2012), reducing the strain budget for subduction interface deformation. Furthermore, a strong structural transition occurs between the North and South Islands in Cook Strait, across which major upper crustal faults of the MFS and lower North Island (i.e., Wellington and Wairarapa faults) are not thought to be continuous (e.g., Pondard and Barnes, 2010).

The region surrounding the Kaikōura earthquake rupture has seen several M_w 7+ earthquakes in the short ∼200-year New Zealand historical record and is an area of high seismic activity. In 1848, a magnitude M_w 7.4–7.7 earthquake is thought to have ruptured more than 100 km along the Awatere fault (Grapes *et al.*, 1998; Mason and Little, 2006). Seven years later in 1855, the M_w 8.1+ Wairarapa earthquake struck the lower North Island on the opposite side of Cook Strait. Coseismic strike-slip displacements along the Wairarapa fault during this event ranged up to ∼19 m and are the largest surface displacements globally observed (Rodgers and Little, 2006). The Hope River segment of the Hope fault also ruptured in an M_w 7.0–7.3 earthquake in 1888 (Cowan, 1991).

More recently, the 2010 M_w 7.1 Darfield earthquake (Gledhill *et al.*, 2011) struck ∼120 km south of the Kaikōura earthquake epicenter, and was followed by the destructive M_w 6.2 Christchurch aftershock (Kaiser *et al.*, 2012). Furthermore, in 2013, the M_w 6.6 Cook Strait and the M_w 6.6 Grassmere earthquakes (Holden *et al.*, 2013; Hamling *et al.*, 2014) struck close to the northern extent of the Kaikōura rupture. Both of these regions were still experiencing seismicity above background levels prior to the Kaikōura earthquake.

GEONET DATASETS

The Kaikōura earthquake was well recorded across the GeoNet network of ∼200 weak motion seismometers, ∼260 strong-motion sensors, and ∼200 continuous Global Navigation Satellite System (GNSS). Although the majority of sites are streaming in real time, some data from triggered strong-motion sites very close to the epicenter were delayed due to communication outages. In response to the earthquake, GeoNet has installed an additional 7 continuous GNSS sites and 14 strong-motion sites. These datasets are openly available through the GeoNet website to the public and research community.

GeoNet notifies the public of earthquakes through a mobile application and social media platforms, such as Facebook and Twitter. Earthquake parameters are also automatically posted and updated on the GeoNet website. After the earthquake, these services coped with extremely heavy loads. The website traffic peaked at ∼35, 000 requests per second and ∼250 million hits in the first day. During the first week following the earthquake, the mobile application pushed out 212 million notifications to 350,000 active users.

Felt Rapid reports are also collected by GeoNet both through the website and mobile devices. Within the first hour of the earthquake, there were over 15,000 Felt Rapid reports (a quick cartoon-based report) and over the first month ∼3500 Felt Detailed reports (traditional survey-based reports).

EARTHQUAKE SOURCE

Surface Deformation

Preliminary ground surface rupture mapping, coastal uplift, and geodetic observations are presented in Hamling *et al.* (2017) and summarized here.

Surface rupture mapping is still underway, but to date meter-scale ruptures have been identified on at least 13 faults with sub-meter-scale ruptures on at least 3 additional faults (summarized in Fig. 1). Many of the fault ruptures are complex, particularly in the south, in which a number of ruptures occurred on faults not previously identified as active. The total surface rupture length, measured from the southwestern tip of the Humps fault zone to the northeastern tip of the Needles fault, with two simplified line segments is ∼180 km. Surface displacements are all oblique, mainly transpressional, and the largest displacements measured to date from displaced cultural features (e.g., fences and roads) are on the Kekerengu (up to 10–12 m dextral) and Papatea (up to 5–6 m vertical) faults.

The tsunami associated with the Kaikōura earthquake was generated through deformation of the seabed in the vicinity of Kaikōura. A number of the faults cross the coastline and seafloor ruptures have been identified in offshore surveys on the submarine Needles fault, as well as the Kekerengu, Papatea, and Hundalee faults.

The 2010 version of the New Zealand National Seismic Hazard Model (Stirling *et al.*, 2012) provided the possibility of a combined rupture of dominant faults in the Kaikōura earthquake. Specifically, the model accounts for a combined rupture of the Jordan thrust–Kekerengu–Needles faults in an M_w 7.6 earthquake. However, the Kaikōura earthquake notably ruptured a larger number of faults both north and south of the Hope fault with greater moment release, which was not fully anticipated in the hazard model (unless uncertainties in magnitude estimates were considered).

Uplift has been observed along parts of the coast between where the Hundalee fault goes offshore in the south and Cape Campbell in the north (Fig. 1), a straight line distance of about 100 km (Hamling *et al.*, 2017). The uplift is visible from stranding of rocky shore platforms with rapidly decaying biota including seaweed, crayfish, and paua (abalone). The amount of uplift has been measured using biological markers previously living at or below low-tide level and clearly varies across the faults. The total range is 0.6–4.8 m, with the maximum being in the block between two local strands of the Papatea fault. Other early notable observations are that uplift increases southward from Cape Campbell toward the Kekerengu fault, and

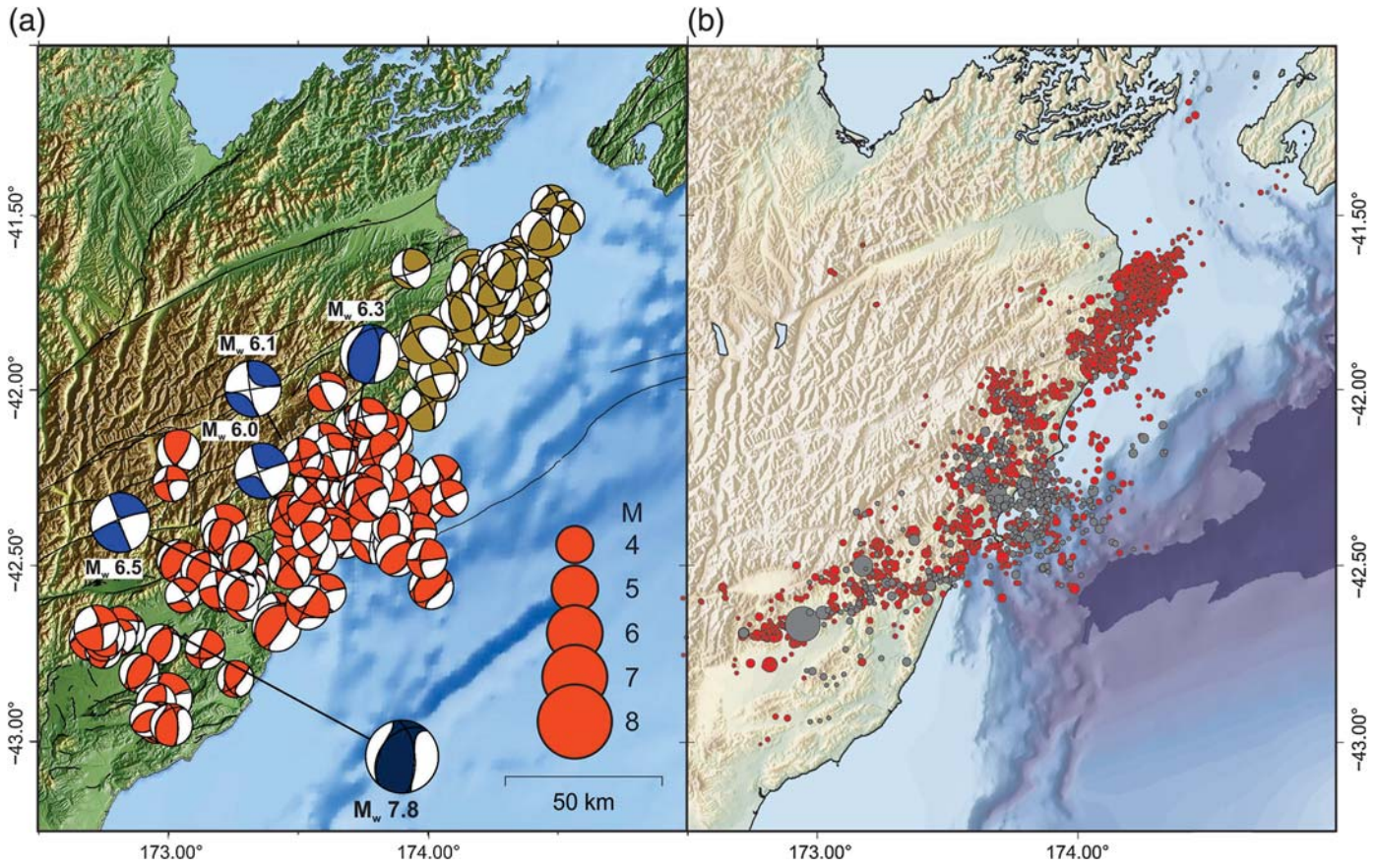

▲ **Figure 2.** (a) Focal mechanisms of the largest aftershocks determined from regional moment tensor inversions based on GeoNet catalog locations. Regional moment tensor solutions for 170 aftershocks ranging between M_w 4.1 and 6.5 with locations and centroid depths (2–28 km) compatible with GeoNet catalog locations. Best-fitting double-couple solutions are overlain on each solution. Two groups of focal mechanisms discussed in the text are shown in red and gold, respectively. (b) Relocated aftershocks from the first 5.5 days (2383 events with magnitude >1.6). Relocations have been calculated using hypoDD (Waldhauser and Ellsworth, 2000; Waldhauser, 2001) and a 1D velocity model approximation to the 3D velocity field (Eberhart-Phillips *et al.*, 2010). Aftershocks are colored according to depth: >25 km shown in gray; <25 km shown in red; note that depths are preliminary.

that uplift at Kaikōura Peninsula was ~0.9 m, consistent with the uplift recorded by the Kaikōura tide gauge (KAIK) and Global Positioning System (GPS) stations.

A complex pattern of coseismic surface displacements has also been captured by Interferometric Synthetic Aperture Radar (InSAR) and GPS (continuous and campaign) data (Hamling *et al.*, 2017). Maximum horizontal displacements of up to 6 m and uplift of up to 2 m were recorded by GPS, whereas InSAR shows that the area affected by the largest displacements moved as much as 10 m horizontally in the Kekerengu area and up to 8 m vertically at the Papatea fault with evidence of widespread anelastic deformation (Hamling *et al.*, 2017).

Source Mechanisms and Aftershocks

The source mechanism of the mainshock determined from Global Centroid Moment Tensor (see Data and Resources) was oblique thrust, in contrast to the largest recorded surface displacements, which were dextral. Mechanisms of ~170+ of the largest aftershocks of the sequence calculated from regional moment tensor inversion are shown in Figure 2. Four aftershocks of $M_w \geq 6.0$ have occurred in the sequence to date, all occurring within the first 14 hours of the mainshock. Three of these have strike-slip mechanisms, with the largest aftershock (M_w 6.5) possibly associated with the Hundalee fault.

Relocated aftershocks from the first 5.5 days following the mainshock (Fig. 2b) show three distinct clusters. A strong SW–NE-striking trend is observed in the southernmost cluster, whereas the central and northern clusters are more diffuse. In general, the aftershock sequence shows a mixture of reverse and strike-slip faulting. The southern and central groups (red in Fig. 2a) show a higher number of reverse-faulting events than strike slip, whereas conversely the northern group (gold in Fig. 2a) shows a higher number of strike-slip-faulting events than reverse.

Earthquake Rupture Process

Fault models being developed for the Kaikōura earthquake are necessarily complex to explain the detailed seismic, geodetic, surface fault rupture, coastal uplift, and tide-gauge datasets.

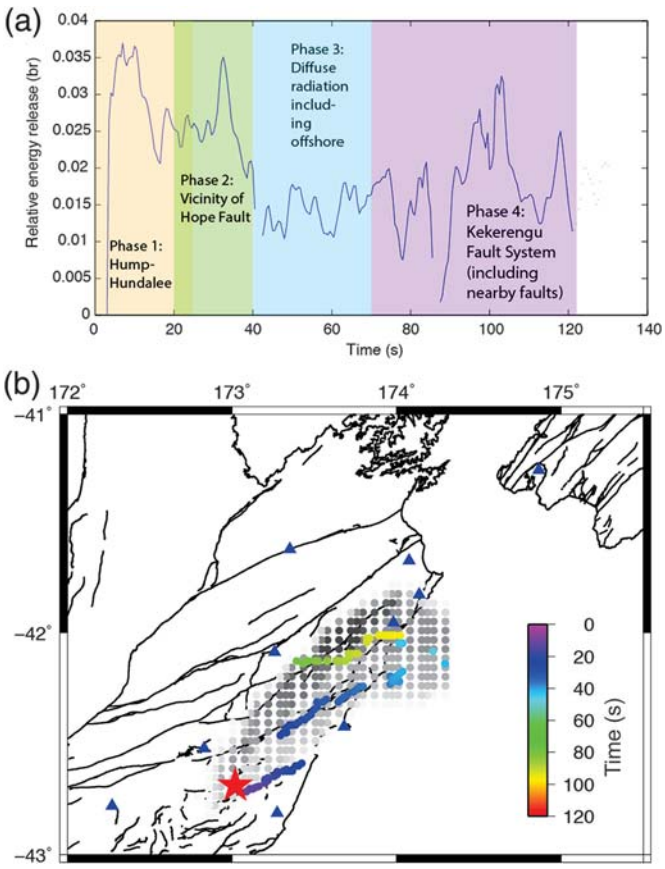

▲ **Figure 3.** Backprojection of energy release during the Kaikōura earthquake for frequencies greater than 0.25 Hz. (a) Source time function from backprojection of strong-motion data plotted as normalized energy at a window centered around each time step from 0 to 120 s. (b) The location of the maximum energy released at any given time step is shown in color. For simplicity, only time steps with energy above a certain normalized threshold are plotted. Gray circles indicate the area of significant backprojected energy release when calculated cumulatively across all depths at that location. Darker gray colors indicate larger relative cumulative values. Strong-motion stations used in the backprojection are shown by blue triangles and the epicenter is shown by a red star.

Geodetic fault models presented in Hamling *et al.* (2017) provide an estimate of the final rupture, and incorporate at least 12 major faults with more than 20 m of slip at depths of ~10 km. Important additional insights into fault interaction and triggering behavior can be gained using the comprehensive strong-motion dataset and new high-rate GPS data to unravel the kinematic evolution of the earthquake rupture.

Preliminary analysis using a backprojection approach to image radiated energy through time shows at least four stages of rupture, including three distinct northeastward-propagating phases of energy release (Fig. 3). A brightness function was calculated from the envelope of velocity waveforms following Kao and Shan (2007) by summing the array response for possible energy release from every model element in a 250 km × 250 km × 39 km volume around the aftershock region. Using frequencies equal to and greater than 0.25 Hz, recorded at local and regional distances, details of the shallow (< 16 km) energy release can be resolved. Figure 3a shows the source time function plotted as normalized energy and Figure 3b shows the location of significant energy release.

The first phase of rupture propagated northeastward from the vicinity of the hypocenter for at least 20 s, with an apparent rupture velocity of < 2 km/s (calculated from the endpoints of each phase of rupture). This phase of rupture likely involved the Humps fault zone and Hundalee fault, then continued offshore during initiation of the second rupture phase at about 20 s after the origin. During the second phase, the maximum energy release jumped to a fault ~25 km to the north, which ruptured toward the NE. This fault rupture continued with a small rightward stepover until at least 40 s, with an apparent rupture velocity of ~2.5 km/s. Interpretations of this phase of rupture are more problematic due to the possible involvement of rupture segments on either side of the Hope fault, as well as the seaward end of the Hope fault itself, where a small amount of surface rupture was observed near the coast. This phase of rupture initiated at a location compatible with the Conway–Charwell fault system, but further analysis is needed to understand the extent of slip along these faults at depth, and their possible interactions.

The third phase at 40–70 s is marked by diffuse energy radiation, some offshore, with no clearly dominant energy release along a single structure. It is not clear from preliminary analysis whether the significant vertical displacement observed on the Papatea fault occurred during this phase of rupture. We note that the absence of a well-constrained coherent rupture front during this phase does not rule out continued simultaneous rupture of multiple segments. We also note that our analysis is sensitive to high-frequency radiation. Several recent events (e.g., Tohoku-Oki) have demonstrated that areas of high-frequency and low-frequency radiation can originate from different locations.

The fourth phase of rupture initiated along a northern east–west-striking structure, possibly the western end of the Fidget fault (Fig. 1). The rupture propagated eastward with a rupture velocity of about 2.5 km/s and a small left stepover. This phase of rupture encompassed the location of the Kekerengu fault, where the largest strike-slip surface offsets were observed (up to 10–12 m dextral).

Two clear separate bursts of energy release are also evident in displacement seismograms, as well as high-rate GPS data shown in Figure 4. GPS stations located near the central and southern parts of the rupture show two dominant displacement pulses clearly separated in time, with ~70-s time delay recorded at the Kaikōura station (KAIK, green in Fig. 4). In the northern rupture area, the two displacement pulses almost overlap, presumably due to northward propagation of the rupture front, and the second pulse is clearly dominant, with peak horizontal displacements of more than 3 m at Cape Campbell (CMBL, light purple in Fig. 4). Although we associate the initial displacement signals with the first two phases of rupture in Figure 3, we associate the second dominant displacement pulse with the northernmost fourth phase of rupture.

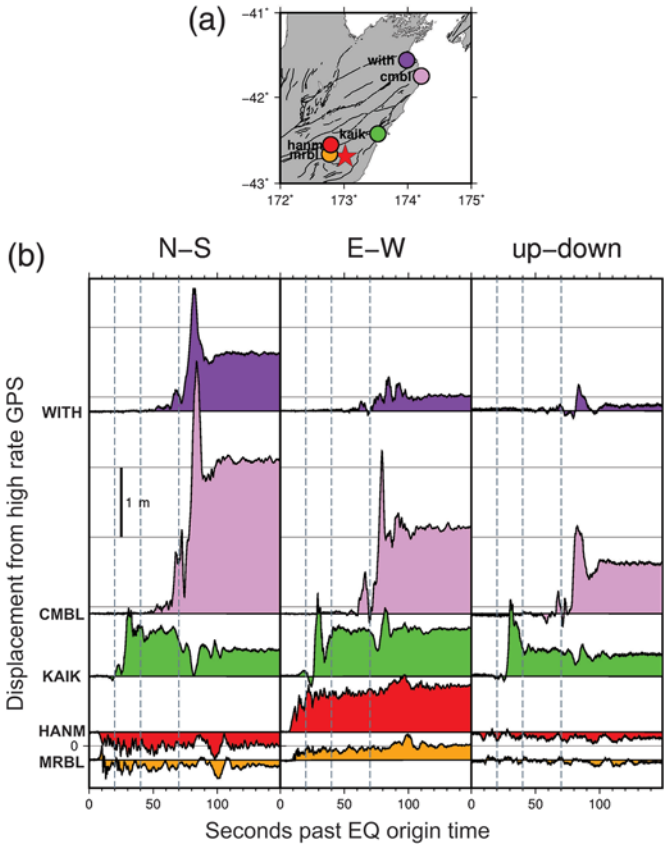

▲ **Figure 4.** (a) Location of high-rate continuous Global Positioning System (GPS) stations in the GeoNet/Land Information New Zealand network within 150 km of the epicenter. (b) High-rate GPS data from stations in (a) showing two distinct displacement pulses. Dashed lines indicate timing of rupture phases imaged from source backprojection in Figure 3. Epoch-by-epoch time series (0.1 s) are obtained with TRACK, the GAMIT/GLOBK module for kinematic processing of GPS data (Herring *et al.*, 2015).

To provide more clarity on the kinematic evolution of the rupture, we have developed a preliminary kinematic slip model based on longer period data (0.1–0.3 Hz; Fig. 5). This model is derived from inversion of kinematic rupture parameters for four fixed fault planes. The predefined fault planes are compatible with the aftershock distribution (Fig. 2b), initial solutions from geodetic data inversions, geological surface rupture observations, and geophysical marine data acquired soon after the earthquake (Hamling *et al.*, 2017). Although the geometry of the fault planes is fixed, the rupture is allowed to start anywhere on the plane. The fault planes are all discretized into subfaults of 1×1 km^2 dimension. We model elliptical distributions of slip (Di Carli *et al.*, 2010) described by nine parameters: the size (two semi-axis lengths) and location (along strike and along dip) of the ellipse, location of rupture starting time (along strike and along dip), rake, maximum slip, and rupture velocity. Synthetic seismograms are computed using the discrete wavenumber approach of Bouchon (1981), using a regional 1D velocity model extracted from Eberhart-Phillips *et al.* (2010).

The resulting kinematic slip solution is broadly compatible with the backprojection results, and shows progressive SW-to-NE failure of key rupture segments. The preferred preliminary model (as defined by the lowest least-squares misfit of the first 200 s of data) favors an almost continuous rupture with each segment failing sequentially. Preliminary testing shows that this model provides a better fit to near-field data than models dominated by deeper rupture of a low-angle fault plane (e.g., preliminary finite-fault models based on global data, see Data and Resources). The progression of the first two rupture segments is similar to the first two phases imaged in the backprojection results. However, the large slip on the third and fourth fault segments, corresponding to the Jordan thrust–Kekerengu–Needles fault rupture initiates at ~47 s earlier than the northernmost rupture phase imaged in backprojection.

Differences between the model results in Figures 3 and 5 during the later phases of rupture could arise for three reasons. First, the pattern of dominant energy release at higher frequencies imaged in the backprojection (> 0.25 Hz) may be different than that at lower frequencies upon which the slip inversion is based (< 0.3 Hz). This would also be compatible with initial slower (or deeper) rupture during the third phase that is not captured in the backprojection results. However, we also note that the pattern of energy release from low-frequency global backprojection (see Data and Resources) is dominated by a single peak initiating at ~60–70 s compatible with the timing of the fourth phase of rupture in Figure 3a. Second, the backprojection may have difficulty isolating simultaneously rupturing segments (e.g., Papatea fault and Jordan thrust which are not clearly associated with any phase in Fig. 3a). This would require complex simultaneous failure of faults in the central part of the rupture, which is consistent with the complex surface rupture patterns in this area and diffuse energy imaged offshore in the backprojection during the third rupture phase. Third, differences could arise from the simplified fault-plane parameterization adopted for the slip inversion, which may map slip associated with additional faults (e.g., thrust faults like the Papatea fault and faults offshore) onto the fixed planes.

In summary, we conclude that the complex rupture in the central section occurs at some time during the period ~45–70 s. It is associated with the initiation of the Kekerengu fault rupture and a second significant pulse of energy release, but is not easily resolved using a single method. Rupture along the Jordan thrust is also likely to have preceded the Kekerengu–Needles fault rupture. Clearly, more complex fault models and further analysis are needed to explain all of the available data, including the numerous observed surface ruptures, and are currently being developed.

GROUND MOTIONS AND STRUCTURAL RESPONSE

The Kaikōura earthquake was well recorded across the GeoNet strong-motion and broadband seismic networks. Horizontal and vertical peak ground accelerations (PGAs) exceeding 1*g* were recorded at both ends of the rupture, at Waiau (station

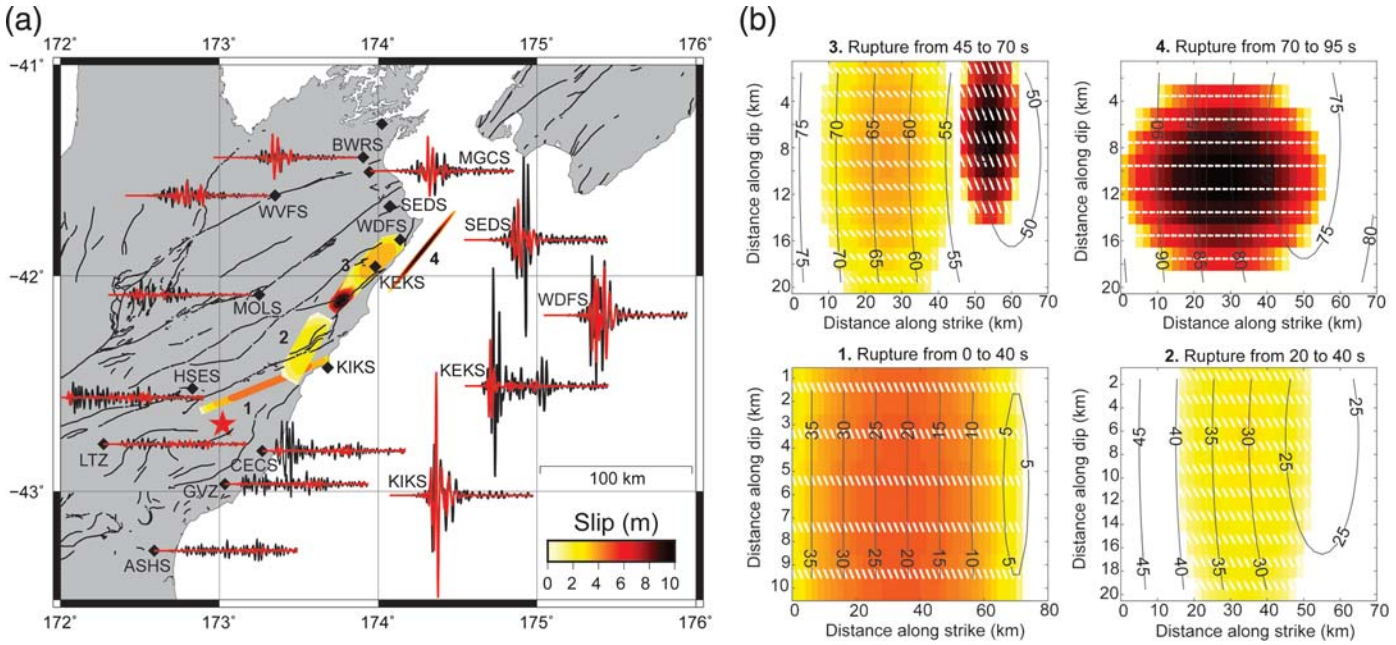

▲ **Figure 5.** Preliminary fault-slip solution (colors indicate slip in meters) based on inversion of strong-motion data on four predefined fault planes (1–4) approximating the Kaikōura rupture. (a) Fault model in map view. We use three-component data from 13 regional strong-motion stations. The acceleration data are integrated into velocity and filtered using a Butterworth band-pass filter from 0.1 to 0.3 Hz (black seismograms). Modeled velocity seismograms are shown in red. (b) Slip solution in plane view for each fault plane. The strike/dip/rake of each fault plane is as follows: 1, 248/61/161; 2, 210/49/149; 3, 226/49/160; and 4, 220/80/180.

WTMC) in the epicentral region as well as Ward (WDFS) ~125 km from the epicenter (Fig. 6). Both of these recording stations were located on deeper soils (Kaiser *et al.*, 2017). Horizontal PGA of over 1*g* was also recorded near Kekerengu Valley (station KEKS), located on rock. The origin of the extremely high vertical PGA of over 3*g* recorded at station WTMC is still under investigation. The strongly asymmetric and periodic character of the record are suggestive of a trampoline effect (e.g., Aoi *et al.*, 2008; Fry *et al.*, 2011). This was also noted in analyses of the record, instrument, and installation location by H. Avery (personal comm., 2016), which concluded that the instrument was functioning correctly. We also note that this instrument was located in a small shed where significant disruption to contents indicated high accelerations occured.

Spectral accelerations exceeded the 500-year return period design level spectra in a number of towns in the upper South Island across a range of spectral periods. Interestingly, the seismometer located on rock (station KIKS) close to the town of Kaikōura recorded relatively modest short-period spectral acceleration and PGA (0.26*g*) compared with other strong-motion stations close to the rupture. However, spectral accelerations and displacements at longer periods greater than 3.5 s were some of the highest recorded. Design-level spectra were also exceeded in parts of the capital city of Wellington in a limited period range of 1–2 s (Fig. 7). Characteristic building damage in the upper South Island and Wellington regions varied due to differences in both ground-shaking characteristics and building stock.

The majority of building damage in the South Island was focused in the small towns of Kaikōura, Waiau, and Ward close to the strongest recorded accelerations. Building stock in the area is predominantly low-rise (1–2 story) timber-frame buildings, with some largely nonresidential buildings of concrete construction. Building damage in these towns was predominantly characterized by out-of-plane failure of loosely tied brick veneers on timber-frame buildings, as well as toppling of masonry chimneys. Only one building, a concrete historic house, collapsed in the earthquake and resulted in a single fatality. Some historic masonry buildings throughout the region were heavily damaged, but did not collapse. As of December 2016, 132 buildings in the upper South Island had been red stickered, meaning they are not safe for re-entry (Canterbury and Marlborough Regional Councils, personal comm., 2016).

In Wellington, spectral accelerations exceeded the current 500-year return period design level spectra (ultimate limit state) in the 1–2 s period range at some recording stations situated on deeper parts of the Wellington sedimentary basin (e.g., the National Museum Te Papa adjacent to the harbor and within the Port area, see Fig. 7). These motions were significantly amplified by factors of 4–6 with respect to rock-site records (Fig. 7). Figure 7 also shows that although the 500-year elastic design spectrum was only exceeded over a limited period range, the inelastic spectrum for a design ductility of three was exceeded over a much broader range. With the long duration of the motions, this suggests that there may have been many cycles of inelastic response to some

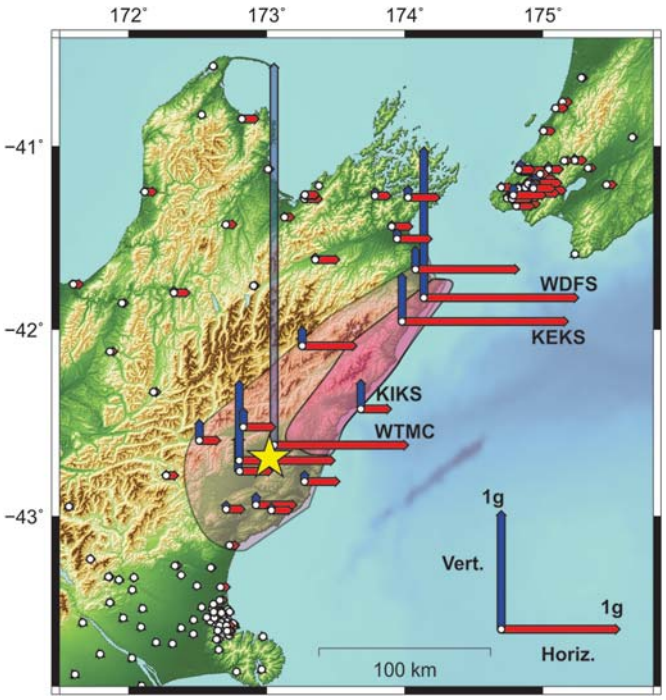

▲ **Figure 6.** Peak ground accelerations in the horizontal (red) and vertical (blue) directions recorded at GeoNet strong-motion stations. Epicenter of the Kaikōura earthquake is shown as a yellow star. Note that the vertical value of over 3*g* recorded at station WTMC (transparent blue bar) has unusual characteristics, which warrant further investigation, as discussed in the text. The approximate extent of mapped landslides is shown as pink shaded area, with the majority occurring in the darker shaded region.

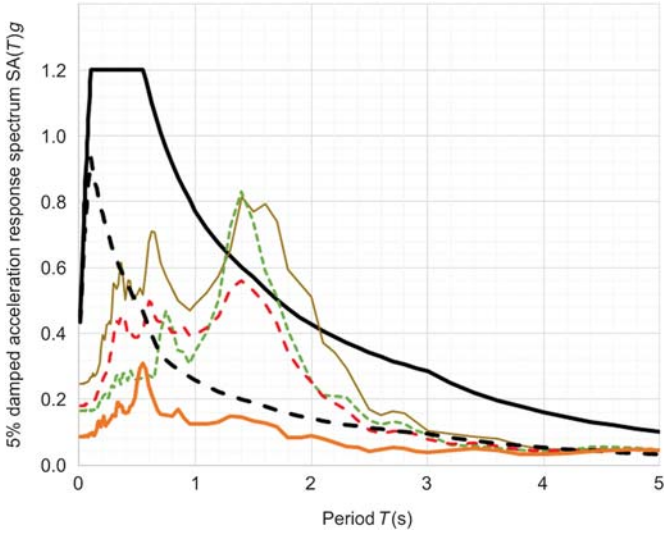

▲ **Figure 7.** Recorded 5% damped acceleration response spectra at two NZS1170.5 class D soft-soil sites (TEPS, green, and CPLB, brown) in the Wellington port area. Also shown is the geometric mean of Wellington NZS1170.5 class D stations (red), the nearby rock site (POTS, orange, class B), and the 500-year NZS1170.5 class D deep- or soft-soil elastic and $\mu = 3$ yield spectra (solid and dashed black lines, respectively). Response spectra are based on the stronger horizontal component, consistent with New Zealand design practice.

structures. Large spectral displacements of around 0.5 m at ~1.5 s period were also observed in the port area. The period range of 1–2 s corresponds approximately to both the fundamental site period of soils in the deeper part of the city basin (Semmens *et al.*, 2010; Kaiser *et al.*, 2017) and the resonant period of mid-rise structures (8–15 story range), in which much of the damage was observed. However, we note that the observed peak spectral accelerations occurred at somewhat larger periods than the site period at many stations. We also note that the south-to-north earthquake rupture terminated ~50–60 km from Wellington and was directed toward the city. Hence, in this location both site/basin and directivity effects were potentially important factors influencing ground motions. Serviceability limit state levels were also exceeded throughout the central city, resulting in damage to nonstructural elements and closure of a significant portion (~10%) of office space three weeks after the earthquake.

PGA in Wellington was moderate (up to 0.28*g*) and similar to those experienced in both M_w 6.6 earthquakes of the Cook Strait sequence (Holden *et al.*, 2013). Ground motions at periods less than 1 Hz were also generally well within 1 in 500-year design level spectra, given that design spectra at shorter periods accommodate the larger motions expected from more proximal earthquake sources (i.e., Wellington fault earthquake). We note that low-rise structures with shorter fundamental periods, including the few hundred unreinforced masonry buildings in the Wellington region, suffered little to no damage during the Kaikōura earthquake.

LANDSLIDE AND TSUNAMI IMPACTS

The Kaikōura earthquake generated tens of thousands of landslides over a total area of about 10,000 km^2, with the majority concentrated in a smaller area of about 3500 km^2 (Fig. 6). The mapped landslide distribution reflects the complexity of the earthquake rupture over a broad area, with the largest landslides occurring either on or adjacent to the faults that ruptured to the surface. A noteworthy aspect of this event is the large number of landslides that occurred on the steep coastal cliffs south of Ward and extending to ~20 km south of Kaikōura leading to the closure of state highway routes. The first limited road access into Kaikōura was possible 11 days after the earthquake, with the northern access route remaining closed months later. Another noteworthy feature of this earthquake is the large number (more than 190) of river-damming landslides it generated. This was partly due to the steep and confined slopes in the area and the widely distributed strong ground shaking.

Given the sparsely populated area affected by landslides, only a few homes were impacted and there were no recorded deaths due to landslides. However, the long-term stability of cracked slopes and landslide dams from future strong earthquakes and significant rain events are an ongoing concern to

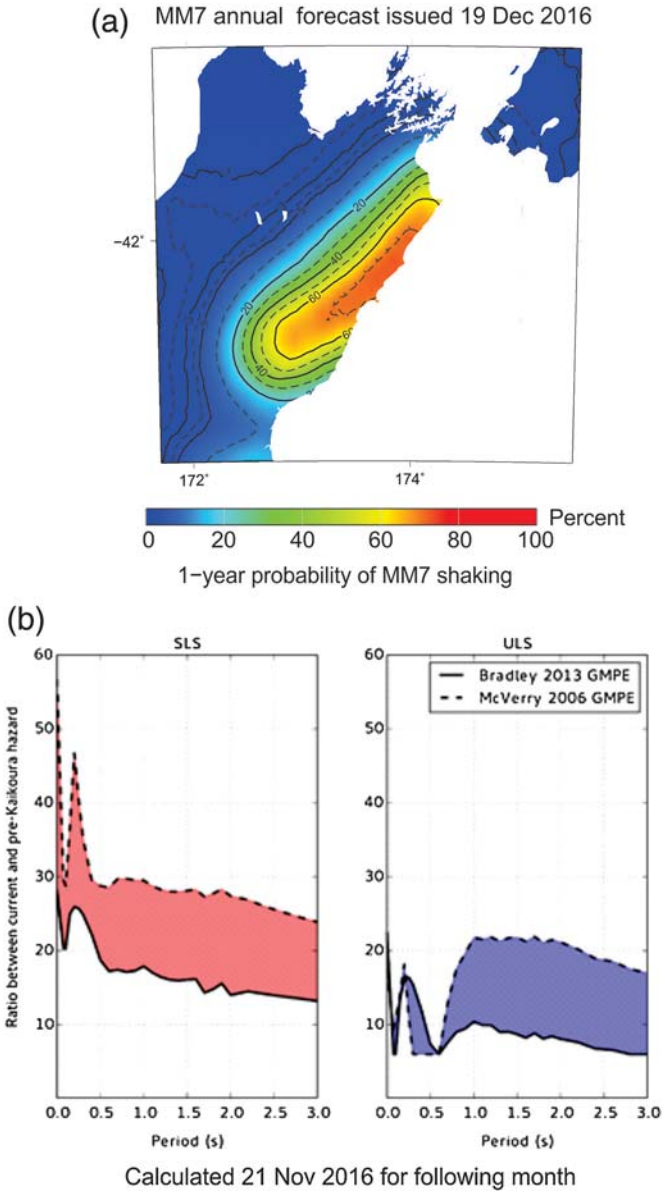

▲ **Figure 8.** Examples of aftershock forecast information provided to the engineering community. (a) Probability of damaging shaking MMI 7 or greater calculated on 19 December 2016 for the following year. (b) The relative increase in probability in Wellington of exceeding the New Zealand building design standard serviceability limit state (SLS; a building likely to continue to be used without repair) and ultimate limit state (ULS; collapse/life safety) spectra based on aftershock forecasts and the ground motion prediction equations of McVerry *et al.* (2006) and Bradley (2013). The forecasts indicate that for a 30-day period starting 21 November 16, Wellington was roughly 15–30 times more likely to experience ground motions that exceeding SLS spectra, and 10–20 times more likely to experience ground motions exceeding ULS spectra than it was prior to the Kaikōura earthquake.

central and local government agencies responsible for rebuilding homes and infrastructure. A particular concern is the potential for debris floods to affect critical downstream residences and infrastructure, should some of the landslide dams breach catastrophically.

Observation of a 2.5 m fall in the level of the GeoNet Kaikōura tide gauge over 24 min prompted a widespread tsunami warning; the reported water level then rose to 1.5 m above normal, though both of these figures are not corrected for ∼1 m of uplift that took place at the gauge location during the earthquake. The tsunami badly damaged a house at Little Pigeon Bay in Banks Peninsula, partially lifting it from its foundations and causing two exterior walls to cave in. In the Kaikōura area, tsunami damage was mitigated by the coseismic uplift of the coast and by the timing of the tsunami close to low tide. A railway bridge at Oaro ∼18 km south of Kaikōura was hit by the tsunami, and has suffered significant damage due to tsunami and/or earthquake shaking. Elsewhere on the Kaikōura coast, debris lines suggest tsunami runup heights of up to about 5 m occurred in some areas, but runup rarely reached above the pre-earthquake storm beach line.

AFTERSHOCK FORECASTS AND FUTURE EARTHQUAKE SCENARIOS

An important part of the response to the Kaikōura earthquake has been the dissemination of information about the potential for aftershocks and other large triggered events. The forecasts (see Data and Resources) are provided in a range of formats including probability and rate tables, descriptive scenarios for future earthquakes, modified Mercalli intensity (MMI) probability maps, and detailed information for government and engineering decision making. An example of forecast information provided to engineers is shown in Figure 8 illustrating (a) the MMI probability and (b) the increase in the forecast 30-day hazard spectra for Wellington compared with the hazard in the same time window prior to the Kaikōura earthquake. To date, the aftershock productivity has been lower than the mean productivity for New Zealand aftershock sequences (D. Pollock, unpublished thesis, 2007; see Data and Resources). The mechanism behind the low productivity is not yet understood, given that aftershock behavior for such large earthquakes is not well constrained due to a paucity of historical aftershock observations from such events.

Using a hybrid model similar to that applied in the Canterbury earthquake sequence (Gerstenberger *et al.*, 2014, 2016; Rhoades *et al.*, 2016), have calculated the forecasts by combining the Short-Term Earthquake Probability (STEP; Gerstenberger *et al.*, 2004, 2005), the Every Earthquake a Precursor According to Scale (EEPAS), and the Proximity to Past Earthquakes (PPE) models (Rhoades and Evison, 2004, 2005, 2006). Hence, this hybrid model combines short, medium, and long-term clustering models. Particular challenges have been (1) the uncertainties due to the lower quality of earthquake catalog data in real time (e.g., Omi *et al.*, 2013), (2) the update of the magnitude to M_w 7.8 two days after the mainshock which resulted in an approximate doubling of the forecast rates from the STEP mean New Zealand model, and (3) the required fast communication and dissemination of results to a wide range of

end users situated over a large aftershock region where forecasts are highly variable in space. For example, the capital city of Wellington is within the region, but has much lower probabilities for damaging shaking from aftershocks than many areas more proximal to the mainshock ruptures (Fig. 8a).

The Kaikōura earthquake triggered widespread slow-slip events (SSEs) on the Hikurangi subduction megathrust immediately after the mainshock which led to concerns about the impact of SSE on future large earthquakes (Gerstenberger *et al.*, 2017; Wallace *et al.*, 2017). Most past studies investigating the relation between seismicity and SSE or aseismic transients have focused on using seismicity to constrain the transients (e.g., Llenos *et al.*, 2009; Llenos and McGuire, 2011; Okutani and Ide, 2011) with few modeling the impact of SSE on future earthquakes (e.g., Mazotti and Adams, 2004). With an expectation from the government of providing quantitative guidance on the potential for large triggered events, a team of scientists from GNS Science and Victoria University subjectively assessed a small increase in likelihood for an $M_w \geq 7.8$ within the next year in central New Zealand; the assessment was informed by probabilities of clustering of large events from the EEPAS model, observed seismicity rate increases during past SSE in New Zealand and by probabilities of $M_w > 7$ clustering from a synthetic seismicity catalog for the region (Robinson *et al.*, 2011).

CONCLUSIONS

The M_w 7.8 Kaikōura earthquake was the largest to strike New Zealand since the 2009 M_w 7.8 Dusky Sound earthquake, and continues a decade of higher than average earthquake impacts. The effects were severe and wide ranging across the upper South Island including two fatalities, a tsunami with local runup heights ranging up to at least 5 m, tens of thousands of landslides of varying size, collapse of one building, and damage to numerous structures in the upper South Island and Wellington.

The earthquake rupture was extremely complex in space and time, rupturing at least 13 separate faults extending from the epicenter in north Canterbury at least ~170 km northward to the vicinity of Cook Strait. The mechanism of the mainshock was oblique thrust, whereas the largest surface ruptures were dextral strike slip. Aftershocks show a mixture of reverse and strike-slip mechanisms. Relocated aftershock locations show three dominant spatial clusters, with seismicity that is more diffuse in the central and northern parts.

Source backprojection of maximum energy release has imaged at least three significant SW-to-NE propagating rupture phases. Preliminary slip models based on strong-motion data and a fixed fault representation are broadly compatible with backprojection results, showing a complex but more continuous south-to-north rupture. The first rupture phase corresponded to essentially continuous rupture of the Humps fault zone–Hundalee fault with the second phase initiating on a structure to the north in the vicinity of the Hope fault around the time that the Hundalee fault rupture extends offshore. The third phase marked by diffuse energy release may have included complex rupture in the central section, followed by initiation of significant fourth phase of rupture ~70 s after the earthquake origin associated with the northern part of the rupture zone in the vicinity of the Kekerengu–Needles faults. This phase also corresponded to a second significant displacement pulse observed in displacement seismograms and high-rate GPS time series.

Ground motions during the earthquake exceeded 1*g* at both ends of the earthquake rupture with damage concentrated in these areas as well as the town of Kaikōura. Differences between the upper South Island and Wellington regions in both ground motions and building stock led to different characteristic damage patterns. Spectral accelerations exceeded 1 in 500-year design level spectra across a range of periods in a number of towns in the upper South Island, where low-rise structures predominate. One in 500-year acceleration and displacement design level spectra were also exceeded in parts of Wellington adjacent to the harbor edge within the critical 1–2 s period range associated with the resonant period of mid-rise structures in which much of the damage was observed. In Wellington, both site effects associated with resonance of the deeper soils in areas adjacent to the harbor edge as well as directivity effects from northward-directed rupture likely had an influence on ground motions in this period range.

GeoNet strong-motion, broadband, geodetic, and tide gauge datasets for the Kaikōura earthquake are freely available and will be crucial in further unraveling details of the complex earthquake rupture. Additional scientific and rapid information has been quickly disseminated via the GeoNet website. Another important part of the response effort has been the provision of information on the likelihood of aftershock forecasts and other large events to the public, government, and engineering communities. Earthquake forecasts have been calculated using a hybrid model which takes into account short, medium, and long-term earthquake clustering. A small increase in likelihood above modeled forecasts for an $M_w \geq 7.8$ has also been included following the observation of multiple triggered SSEs on the Hikurangi subduction interface, which presented a particular challenge to forecasting methods.

DATA AND RESOURCES

GeoNet seismic, continuous Global Navigation Satellite System, and tide gauge data, as well as the earthquake and moment tensor catalog are openly available through the GeoNet website (www.geonet.org.nz, last accessed March 2017). Processed strong-motion data (spectral acceleration, velocity, and displacement) and site parameters are openly available from the New Zealand Strong-Motion Database (http://info.geonet.org.nz/x/TQAdAQ, last accessed March 2017; Kaiser *et al.*, 2017; Van Houtte *et al.*, 2017). Data from high-rate continuous Global Positioning System stations of the GeoNet/Land Information New Zealand network are available upon request from E. D. Earthquake relocations are available upon request to S. B. Surface rupture and coastal uplift data summarized here have been collected by teams from GNS Science, National Institute of

Water and Atmospheric Research Ltd., Victoria University of Wellington, University of Canterbury, University of Canterbury, and University of Otago and are presented in Hamling *et al.* (2017). The update M_w for the Dusky Sound earthquake was adopted from www.earthquake.usgs.gov (last accessed March 2017). Global Centroid Moment Tensor is available at www.globalcmt.org (last accessed January 2017). An early version of the finite-fault model solution based on global data was obtained at https://earthquake.usgs.gov/earthquakes/eventpage/us1000778i#finite-fault (last accessed December 2017). Low-frequency global backprojection results are available at http://ds.iris.edu/spud/backprojection/13297540 (last accessed January 2017). GeoNet ShakeMap for the Kaikōura earthquake is available at http://info.geonet.org.nz/x/joA5AQ (last accessed March 2017). Current aftershock forecasts are available through GeoNet at http://info.geonet.org.nz/x/ZwBAAQ (last accessed March 2017). Some figures were made using Generic Mapping Tools (www.soest.hawaii.edu/gmt, last accessed January 2017; Wessel and Smith 1998). The unpublished thesis by D. Pollock (2007). Aspects of short-term and long-term seismic hazard assessment in New Zealand, ETH Zurich, Zurich, Switzerland.

ACKNOWLEDGMENTS

This work was supported by public research funding from the Government of New Zealand. These preliminary findings would not be possible without the crucial data provided by GeoNet with the support of its sponsors New Zealand Earthquake Commission (EQC), GNS Science, and Land Information New Zealand. We would like to thank GeoNet staff, including field and data system technicians and the public information team. Although this article focuses on seismological aspects of the response, we acknowledge contributions from the wider response team from GNS Science, National Institute of Water and Atmospheric Research Ltd., New Zealand universities, private practice, and international collaborators. Particular thanks go to the fault rupture and deformation mapping teams including Pilar Villamor, Russ Van Dissen, Robert Langridge, David Barrell, Timothy Little, Andrew Nicol, Jarg Pettinga, Julie Rowland, Mark Stirling, Jamie Howarth, Phaedra Upton, and William Ries (on-land surface ruptures and uplift); Philip Barnes (submarine surface rupture mapping); Marlene Villeneuve, Sam McColl, Simon Cox, Dougal Townsend, Brenda Rosser, Corrine Singeisen, Barbara Lyndsell, Fernando Della Pasqua, Garth Archibald, Biljana Lukovic, Katie Jones, Jonathan Davidson, the Geotechnical Extreme Events Reconnaissance (GEER) team, and U.S. Geological Survey (landslide mapping). We also greatly thank Honn Kao (Natural Resources Canada) for use of his backprojection code, Hamish Avery (Canterbury Seismic Instruments Ltd.) for analysis of the WTMC record and Sigrun Hreinsdottir for helpful comments on the article. We are grateful to two anonymous reviewers and Editor Zhigang Peng for prompt and constructive reviews of this article. A short preliminary version of this article was prepared for printed proceedings of Seminar Nasional Pengurangan Risiko Bencana, 14–17 February 2017, Yogyakarta.

REFERENCES

Aoi, S., T. Kunugi, and H. Fujiwara (2008). Trampoline effect in extreme ground motion, *Science* **322,** no. 5902, 727–730.

Beavan, J., L. M. Wallace, N. Palmer, P. Denys, S. Ellis, N. Fournier, S. Hreinsdottir, C. Pearson, and M. Denham (2016). New Zealand GPS velocity field: 1995–2013, *New Zeal. J. Geol. Geophys.* **59,** no. 1, 5–14.

Bouchon, M. (1981). A simple method to calculate Green's functions for elastic layered media, *Bull. Seismol. Soc. Am.* **71,** no. 4, 959–971.

Bradley, B. A. (2013). A New Zealand-specific pseudo-spectral acceleration ground-motion prediction equation for active shallow crustal earthquakes based on foreign models, *Bull. Seismol. Soc. Am.* **103,** no. 3, 1801–1822.

Cowan, H. A. (1991). The north Canterbury earthquake of September 1, 1888, *J. Roy. Soc. New Zeal.* **21,** 1–12.

Di Carli, S., C. François-Holden, S. Peyrat, and R. Madariaga (2010). Dynamic inversion of the 2000 Tottori earthquake based on elliptical subfault approximations, *J. Geophys. Res.* **115,** no. B12328, doi: 10.1029/2009JB006358.

Eberhart-Phillips, D., and S. Bannister (2010). 3-D imaging of Marlborough, New Zealand, subducted plate and strike-slip fault systems, *Geophys. J. Int.* **182,** no. 1, 73–96, doi: 10.1111/j.1365-246X.2010.04621.x.

Eberhart-Phillips, D., M. E. Reyners, S. C. Bannister, M. P. Chadwick, and S. M. Ellis (2010). Establishing a versatile 3-D seismic velocity model for New Zealand, *Seismol. Res. Lett.* **81,** no. 6, 992–1000, doi: 10.1785/gssrl.81.6.992.

Fry, B., S. C. Bannister, R. J. Beavan, L. Bland, B. A. Bradley, S. C. Cox, W. J. Cousins, N. H. Gale, G. T. Hancox, C. Holden, *et al.* (2010). The M_w 7.6 Dusky sound earthquake of 2009: Preliminary report, *Bull. New Zeal. Soc. Earthq. Eng.* **43,** no. 1, 24–40.

Fry, B., R. A. Benites, and A. E. Kaiser (2011). The character of accelerations in the M_w 6.2 Christchurch earthquake, *Seismol. Res. Lett.* **82,** no. 6, 846–852, doi: 10.1785/gssrl.82.6.846.

Gerstenberger, M., G. McVerry, D. Rhoades, and M. Stirling (2014). Seismic hazard modeling for the recovery of Christchurch, *Earthq. Spectra* **30,** no. 1, 17–29, doi: 10.1193/021913EQS037M.

Gerstenberger, M., L. Wallace, and B. Fry (2017). Earthquake forecast modelling for the M_w 7.8 Kaikōura earthquake and triggered slow slip events, Abstract submitted to the *Annual Meeting of the Seismological Society of America*, Denver, Colorado, 17–21 April 2017.

Gerstenberger, M. C., D. A. Rhoades, and G. H. McVerry (2016). A hybrid time-dependent probabilistic seismic-hazard model for Canterbury, New Zealand, *Seismol. Res. Lett.* **87,** no. 6, 1311–1318.

Gerstenberger, M. C., S. Wiemer, and L. Jones (2004). Real-time forecasts of tomorrow's earthquakes in California: A new mapping tool, *Denver, Colorado, U.S. Geol. Surv. Open-file Rept.2004-1390*, 39 pp.

Gerstenberger, M. C., S. Wiemer, L. M. Jones, and P. A. Reasenberg (2005). Real-time forecasts of tomorrow's earthquakes in California, *Nature* **435,** no. 7040, 328–331.

Gledhill, K. R., J. Ristau, M. E. Reyners, B. Fry, and C. Holden (2011). The Darfield (Canterbury, New Zealand) M_w 7.1 earthquake of September 2010: A preliminary seismological report, *Seismol. Res. Lett.* **82,** no. 3, 378–386.

Grapes, R., T. Little, and G. Downes (1998). Rupturing of the Awatere fault during the 1848 October 16 Marlborough earthquake, *New Zeal. J. Geol. Geophys.* **41,** 387–399.

Hamling, I. J., S. Hreinsdóttir, K. Clark, J. Elliott, C. Liang, E. Fielding, N. Litchfield, P. Villamor, L. Wallace, T. J. Wright, *et al.* (2017). Complex multi-fault rupture during the 2016 M_w 7.8 Kaikōura earthquake, New Zealand, *Science* eaam7194, doi: 10.1126/science.aam7194.

Hamling, I. J., E. D'Anastasio, L. M. Wallace, S. M. Ellis, M. Motagh, S. Samsonov, N. G. Palmer, and S. Hreinsdottir (2014). Crustal deformation and stress transfer during a propagating earthquake sequence: The 2013 Cook Strait sequence, central New Zealand, *J. Geophys. Res.* **119,** no. 7, 6080–6092.

Herring, T. A., R. W. King, M. A. Floyd, and S. C. McClusky (2015). *Introduction to GAMIT/GLOBK, Release 10.6*, Massachusetts Institution of Technology, Cambridge, Massachusetts.

Holden, C., A. E. Kaiser, R. J. Van Dissen, and R. Jury (2013). Sources, ground motion and structural response characteristics in Wellington of the 2013 Cook Strait earthquakes, *Bull. New Zeal. Soc. Earthq. Eng.* **46,** no. 4, 188–195.

Kaiser, A. E., C. Holden, R. J. Beavan, R. D. Beetham, R. A. Benites, A. Celentano, D. Collet, W. J. Cousins, M. Cubrinovski, G. D. Dellow, *et al.* (2012). The M_w 6.2 Christchurch earthquake of February 2011: Preliminary report, *New Zeal. J. Geol. Geophys.* **55,** no. 1, 67–90.

Kaiser, A. E., C. Van Houtte, N. D. Perrin, L. Wotherspoon, and G. H. McVerry (2017). Site characterisation of GeoNet stations for the New Zealand Strong Motion Database, *Bull. New Zeal. Soc. Earthq. Eng.*, **50,** no. 1, 39–49.

Kao, H., and S.-J. Shan (2007). Rapid identification of earthquake rupture plane using source-scanning algorithm, *Geophys. J. Int.* **168,** no. 3, 1011–1020.

Langridge, R. M., J. Campbell, N. L. Hill, V. Pere, J. Pope, J. Pettinga, B. Estrada, and K. Berryman (2003). Paleoseismology and slip rate of the Conway Segment of the Hope fault at Greenburn Stream, South Island, New Zealand, *Ann. Geophys.* **46,** 1119–1139.

Langridge, R. M., W. F. Ries, N. J. Litchfield, P. Villamor, R. J. Van Dissen, D. J. A. Barrell, M. S. Rattenbury, D. W. Heron, S. Haubrock, D. B. Townsend, *et al.* (2016). The New Zealand active faults database, *New Zeal. J. Geol. Geophys.* **59,** no. 1, 86–96.

Litchfield, N. J., R. Van Dissen, R. Sutherland, P. M. Barnes, S. C. Cox, R. Norris, R. J. Beavan, R. Langridge, P. Villamor, K. Berryman, *et al.* (2014). A model of active faulting in New Zealand, *New Zeal. J. Geol. Geophys.* **57,** 32–56.

Llenos, A. L., and J. J. McGuire (2011). Detecting aseismic strain transients from seismicity data, *J. Geophys. Res.* **116,** no. B6, doi: 10.1029/2010JB007537.

Llenos, A. L., J. J. McGuire, and Y. Ogata (2009). Modeling seismic swarms triggered by aseismic transients, *Earth Planet. Sci. Lett.* **281,** no. 1, 59–69.

Mason, D. P. M., and T. A. Little (2006). Refined slip distribution and moment magnitude of the 1848 Marlborough earthquake, Awatere fault, New Zealand, *New Zeal. J. Geol. Geophys.* **49,** no. 3, 375–382.

Mazzotti, S., and J. Adams (2004). Variability of near-term probability for the next great earthquake on the Cascadia subduction zone, *Bull. Seismol. Soc. Am.* **94,** no. 5, 1954–1959.

McVerry, G. H., J. X. Zhao, N. A. Abrahamson, and P. G. Somerville (2006). New Zealand acceleration response spectrum attenuation relations for crustal and subduction zone earthquakes, *Bull. New Zeal. Soc. Earthq. Eng.* **39,** no. 1, 1–58.

Norris, R. J., and A. F. Cooper (2007). The Alpine Fault, New Zealand; surface geology and field relationships, in *A Continental Plate Boundary: Tectonics at South Island, New Zealand*, D. Okaya, T. Stern, and F. J. Davey (Editors), American Geophysical Union, Geophysical Monograph Series 175, 157–175.

Okutani, T., and S. Ide (2011). Statistic analysis of swarm activities around the Boso Peninsula, Japan: Slow slip events beneath Tokyo Bay?, *Earth Planets Space* **63,** no. 5, 419–426.

Omi, T., Y. Ogata, Y. Hirata, and K. Aihara (2013). Forecasting large aftershocks within one day after the main shock, *Sci. Rept.* **3**.

Pondard, N., and P. M. Barnes (2010). Structure and paleoearthquake records of active submarine faults, Cook Strait, New Zealand: Implications for fault interactions, stress loading, and seismic hazard, *J. Geophys. Res.* **115,** no. B12320, doi: 10.1029/2010JB007781.

Rhoades, D. A., and F. F. Evison (2004). Long-range earthquake forecasting with every earthquake a precursor according to scale, *Pure Appl. Geophys.* **161,** no. 1, 47–72.

Rhoades, D. A., and F. F. Evison (2005). Test of the EEPAS forecasting model on the Japan earthquake catalogue, *Pure Appl. Geophys.* **162,** nos. 6/7, 1271–1290.

Rhoades, D. A., and F. F. Evison (2006). The EEPAS forecasting model and the probability of moderate-to-large earthquakes in central Japan, *Tectonophysics* **417,** nos. 1/2, 119–130.

Rhoades, D. A., M. Liukis, A. Christophersen, and M. C. Gerstenberger (2016). Retrospective tests of hybrid operational earthquake forecasting models for Canterbury, *J. Geophys. Res.* **204,** no. 1, 440–456, doi: 10.1093/gji/ggv447.

Robinson, R., R. Van Dissen, and N. Litchfield (2011). Using synthetic seismicity to evaluate seismic hazard in the Wellington region, New Zealand, *Geophys. J. Int.* **187,** no. 1, 510–528.

Rodgers, D. W., and T. A. Little (2006). World's largest coseismic strike-slip offset: The 1855 rupture of the Wairarapa fault, New Zealand, and implications for displacement/length scaling of continental earthquakes, *J. Geophys. Res.* **111,** no. B12408.

Semmens, S., N. D. Perrin, and G. D. Dellow (2010). It's Our Fault: Geological and geotechnical characterisation of the Wellington central business district, *GNS Science Consultancy Rept. 2010/176*, 48 pp.+ 1 CDStandards NZ 2004

Smith, W. D. (1981). The vast event—How vast and how often? in *Large Earthquakes in New Zealand. Miscellaneous Series No. 5*, M. M. Creswell (Compiler), The Royal Society of New Zealand, Wellington, New Zealand, 17–23.

Stirling, M. W., G. H. McVerry, M. C. Gerstenberger, N. J. Litchfield, R. J. Van Dissen, K. R. Berryman, P. Barnes, L. M. Wallace, P. Villamor, R. M. Langridge, *et al.* (2012). National Seismic Hazard Model for New Zealand: 2010 update, *Bull. Seismol. Soc. Am.* **102,** no. 4, 1514–1542, doi: 10.1785/0120110170.

Sutherland, R., K. Berryman, and R. Norris (2006). Quaternary slip rate and geomorphology of the Alpine fault: Implications for kinematics and seismic hazard in southwest New Zealand, *Geol. Soc. Am. Bull.* **118,** no. 3/4, 464–474.

Van Dissen, R., and R. S. Yeats (1991). Hope fault, Jordan thrust, and uplift of the Seaward Kaikoura Range, New Zealand, *Geology* **19**, 393–396, doi: 10.1130/0091-7613(1991)019<0393:HFJTAU>2.3.CO;2.

Van Houtte, C., S. Bannister, C. Holden, S. Bourguignon, and G. McVerry (2017). The New Zealand strong motion database, *Bull. New Zeal. Soc. Earthq. Eng.* **50,** no. 1, 1–20.

Waldhauser, F. (2001). HypoDD: A computer program to compute double-difference hypocenter locations, *U.S. Geol. Surv. Open-File Rept. 01-113*, 25 pp.

Waldhauser, F., and W. L. Ellsworth (2000). A double-difference earthquake location algorithm: Method and application to the northern Hayward fault, California, *Bull. Seismol. Soc. Am.* **90,** 1353–1368.

Wallace, L., Y. Kaneko, E. D'Anastasio, S. Hreinsdottir, N. Bartlow, B. Fry, Z. Peng, I. Hamling, and M. Gerstenberger (2017). Widespread slow slip events triggered at the Hikurangi subduction zone by the M 7.8 Kaikoura earthquake, New Zealand, Abstract submitted to the *JpGU-AGU Joint Meeting*, Tokyo, Japan, 20–25 May 2017.

Wallace, L. M., P. Barnes, J. Beavan, R. Van Dissen, N. Litchfield, J. Mountjoy, R. Langridge, G. Lamarche, and N. Pondard (2012). The kinematics of a transition from subduction to strike-slip: An example from the central New Zealand plate boundary, *J. Geophys. Res.* **117,** no. B02405, doi: 10.1029/2011JB008640.

Wallace, L. M., M. E. Reyners, U. A. Cochran, S. C. Bannister, P. M. Barnes, K. R. Berryman, G. L. Downes, D. Eberhart-Phillips, A. Fagereng, S. M. Ellis, *et al.* (2009). Characterizing the seismogenic zone of a major plate boundary subduction thrust: The Hikurangi Margin, New Zealand, *Geochem. Geophys. Geosys.* **10,** no. 10, Q10006, doi: 10.1029/2009GC002610.

Wessel, P., and W. H. F. Smith (1998). New, improved version of the generic mapping tools released, *EOS Trans. AGU* **79,** 579.

A. Kaiser
N. Balfour
B. Fry
C. Holden
N. Litchfield
M. Gerstenberger
E. D'Anastasio
N. Horspool
G. McVerry
J. Ristau
S. Bannister
A. Christophersen
K. Clark
W. Power
D. Rhoades
C. Massey
I. Hamling
L. Wallace
Y. Kaneko
R. Benites
C. Van Houtte[1]
S. Dellow
K. Gledhill
GNS Science
P.O. Box 30-368
Lower Hutt 5040
New Zealand
a.kaiser@gns.cri.nz
e.danastasio@gns.cri.nz
s.bannister@gns.cri.nz

J. Mountjoy
National Institute of Water and Atmospheric Research Ltd. (NIWA)
Private Bag 14901
Wellington 6241
New Zealand

L. Wotherspoon
K. Elwood
Faculty of Engineering
University of Auckland
Private Bag 92019
Auckland 1142
New Zealand

Published Online 5 April 2017

[1] Also at Department of Earth and Planetary Sciences, Harvard University, Cambridge, Massachusetts 02138 U.S.A.